Dominant Kitaev interactions in the honeycomb materials $Na_3Co_2SbO_6$ and $Na_2Co_2TeO_6$

Alaric L. Sanders,[1] Richard A. Mole,[2] Jiatu Liu,[3] Alex J. Brown,[3] Dehong Yu,[2] Chris D. Ling,[3] and Stephan Rachel[1,*]

[1]*School of Physics, University of Melbourne, Parkville, VIC 3010, Australia*

[2]*Australian Nuclear Science and Technology Organisation (ANSTO), New Illawarra Road, Lucas Heights, New South Wale 2234, Australia*

[3]*School of Chemistry, The University of Sydney, Sydney, NSW 2006, Australia*

(Received 30 December 2021; revised 22 June 2022; accepted 23 June 2022; published 20 July 2022)

Cobaltates with 3*d* based layered honeycomb structure were recently proposed as Kitaev magnets and putative candidates to host the long-sought Kitaev spin liquid. Here we present inelastic neutron scattering results down to 50 mK for powder samples of $Na_3Co_2SbO_6$ and $Na_2Co_2TeO_6$, with high resolution in regions of low momentum and energy transfers. We compare the experimental data below the antiferromagnetic zigzag ordering temperature with dynamical structure factors obtained within spin wave theory. We search the wide parameter range of a K-J_1-Γ-Γ'-J_3 spin 1/2 model and identify the best fits to constant momentum cuts of the inelastic neutron data. The powder average limits our ability to uniquely select a best-fit model, but we find that the experimental data is matched equally well by two classes of parameters: one with a dominant $K < 0$, $|K/J_1| \sim 5 \ldots 25$, and another with $K > 0$, $|K/J_1| \sim 1$. We show that these classes are equivalent under the exact self-duality transformation identified by Chaloupka and Khalliulin [Phys. Rev. B **92**, 024413 (2015)]. This model symmetry unifies a number of previous parameter estimates. Though the two cases are indistinguishable by our experiment, there is evidence in favor of the $K < 0$ case. A purely isotropic Heisenberg model is incompatible with our results.

DOI: 10.1103/PhysRevB.106.014413

I. INTRODUCTION

The search for quantum spin liquids (QSLs) is one of the great challenges in the field of strongly correlated electrons [1–5]. A QSL state possesses short-ranged magnetic fluctuations but no long-range order. It is, hence, a featureless state which is mostly characterized by the absence of clear and easily-identifiable features. Despite many years of extensive research, few candidate spin liquid materials are known [6–8], and the list of theory proposals for experimental realisations is rather short. Mott insulators with geometric or spin-exchange frustration are the traditional places to search for QSLs [3]. As an additional complication, in two and three spatial dimensions models for QSLs can usually not be solved exactly and theoreticians rely on approximate numerical methods to identify and characterize such states.

Kitaev's seminal work opened an alternative avenue, where he introduced an exactly soluble QSL Hamiltonian with bond-dependent Ising interactions on the honeycomb lattice [9]. The exact solution revealed that the QSL consists of free Majorana fermions coupled to a static $\mathbb{Z}_2$ gauge field, nicely illustrating the fractionalization of the original spin degrees of freedom.

This purely theoretical development was further fueled by the influential work by Jackeli and Khaliullin [10] who proposed that Kitaev model might be realized in transition metal oxides with strong spin-orbit coupling. The idea is based on an observation that the exchange interactions between spin-orbital entangled moments are highly anisotropic and also depend on the bond directions [11]. For a pedagogical review about spin-orbit entangled states of matter see Ref. [12]. The first Kitaev candidate material was Na_2IrO_3 [13,14] along with its sister compound α-Li_2IrO_3 [15], which both turned out to be magnetically ordered at low temperatures. Despite this setback, subsequent work substantiated the claim that these iridates possess non-negligible Kitaev spin interactions along with other generic spin exchange [16–39].

The second wave of experiments focused on α-$RuCl_3$. While its low-temperature phase revealed magnetic long-range order of the zigzag type [40] just like Na_2IrO_3, its excitation spectrum measured with inelastic neutrons was interpreted as a combination of magnons stemming from the magnetic order and additional features due to the system's proximity to a QSL [37,41–44]. A milestone was the report of a quantized thermal conductance when a magnetic field is applied to α-$RuCl_3$ [45,46]: the measured conductance plateau is in agreement with a chiral Majorana mode as expected from Kitaev's model with applied magnetic field (corresponding to a non-Abelian QSL) [9]. It is generally thought that the generic spin exchange spoiling the QSL state in zero field needs to be suppressed by a sufficiently strong magnetic field, until the remaining compass interactions can dominate and cause the non-Abelian QSL state to prevail.

A major challenge in obtaining a better theoretical understanding is to identify the details of the generic *non-Kitaev* interactions in the candidate materials. However, not even the strength and sign of the Kitaev compass interactions are known with certainty. Experimental determination of these coupling constants is necessarily indirect. Previous estimates have come from magnetic susceptibility

*Corresponding author: stephan.rachel@unimelb.edu.au

TABLE I. Best fit model parameters for $Na_2Co_2TeO_6$ and $Na_3Co_2SbO_6$, from present literature and our work. ± on the labels refer to the sign of K. (⋆ This model also includes a small interlayer Heisenberg coupling, which we neglect.)

$Na_2Co_2TeO_6$		J	K	Γ	Γ′	J_2	J_3
ta–	[53]	−0.1	−9	1.8	0.3	0.3	0.9
tb–	[54]	−0.1	−7.4	−0.1	0.05	0	1.4
tb+	[54]	−1.5	3.3	−2.8	2.1	0	1.5
tc–	[55]⋆	−0.2	−7	0.02	−0.23	0.05	1.2
tc+	[55]⋆	−3.2	2.7	−2.9	1.6	0.1	1.2
td	[68]	−2.32	0.125	0.125	0	0	2.5
tx–	this work	−0.2	−7.0	0.5	0.15	0	1.6
tx+	this work	−3.5	3.2	−3.0	2	0	1.4
$Na_3Co_2SbO_6$		J	K	Γ	Γ′	J_2	J_3
sa–	[53]	−2.0	−9	0.3	−0.8	0	0.8
sb–	[54]	−2.1	−4	−0.7	0.6	0	1.2
sb+	[54]	−4.7	3.6	1.3	−1.4	0	0.95
sx–	this work	−1.4	−10	−0.3	−0.6	0	0.6
sx+	this work	−5	2	−4	0.3	0	0.6

measurements [44,47,48], Raman spectroscopy [49], x-ray scattering [28,50,51], and most commonly, inelastic neutron scattering (INS) [16,41,52–55]. Theoretical determination of these coupling constants is a very subtle task, ultimately relying on density functional theory [24,30,42,56–62].

While most attention was given to the iridates and ruthenates of d^5 ions Ir^{4+} and Ru^{3+}, respectively, a recent proposal emphasized that cobaltates of d^7 ions such as Co^{2+} might be another platform for Kitaev candidate materials with pseudospin-$\frac{1}{2}$ [62–64], despite some skepticism that spin-orbit coupling is insufficient to promote compass interactions. The first series of experimental results including $Na_2Co_2TeO_6$ and $Na_3Co_2SbO_6$ confirmed that their low-temperature phase is again antiferromagnetically zigzag-ordered [65–67]. Spin-wave theory modeling of neutron scattering data has suggested that Heisenberg-Kitaev type models can capture the low energy physics in the materials [53–55,59,68,69], however, the community is yet to reach a consensus as to the sign and magnitude of the Kitaev interaction (see Table I).

Here we present INS results for $Na_3Co_2SbO_6$ and $Na_2Co_2TeO_6$. Our data was measured at temperatures as low as 50 mK, a regime which was not accessed in any previous experiments. Moreover, in order to complement the excellent experimental data already available for both compounds [53–55,68], we provide high resolution data in regions of low momentum and energy transfers. The elastic signal in our measurements is as low as 0.2 meV, an energy regime which was previously only reached for $Na_2Co_2TeO_6$ [68] but not for $Na_3Co_2SbO_6$. While our data does not reveal novel physics at these low temperatures or energy transfers, it is crucial to test these regimes in order to rule out any overlooked phases or phenomena. We model the dynamical structure factor within spin wave theory, and show that a purely isotropic J_1–J_2–J_3 model is *incompatible* with the experimental data. By fitting our model to our experimental data we show that best fits are obtained for extended Heisenberg-Kitaev models with either ferro- or antiferromagnetic Kitaev exchange K. This ambiguity in the powder samples was observed before [55,68], and we will show that this is in fact expected due to an exact self-duality transformation identified by Chaloupka and Khalliulin [31]. Good quality data is available in regions of large momentum and energy transfer [53–55,68], which have established that Kitaev type models are capable of capturing a majority of features seen in the powder averaged inelastic spectrum.

By concentrating on the excitations close to zero energy, we are able to perform an accurate indirect measurement of the energy gap, which in turn establishes a constraint on the values of the symmetry breaking Γ, Γ′ terms. We argue that the most likely scenario for both materials is a dominant ferromagnetic $K < 0$ with $|K/J_1|$ being in the range $5 - 25$. Hence, our results indicate that perturbing the magnetically ordered ground state by strain [70,71], pressure [37] or an applied magnetic field [45,56] would be an exciting attempt to push the material into the QSL phase.

The paper is organized as follows. In Sec. II we discuss the sample preparation of the materials used in Sec. III to perform INS experiments. In Sec. IV we perform linear spin wave theory and derive the scattering intensity which we fit to the experimental data in Sec. V. In the discussion in Sec. VI, we elaborate on a model duality between ferromagnetic and antiferromagnetic K in agreement with our best fits. Next, we argue that both excitation spectra are gapped, albeit with a much smaller gap for $Na_2Co_2TeO_6$ as previously reported. We discuss the classical ground states and the corresponding spin quantization axis, and elaborate on predictions for single crystal measurements. The paper ends with a conclusion in Sec. VII.

II. SAMPLE PREPARATION

The same polycrystalline sample of $Na_3Co_2SbO_6$ was used in this work as in Wong *et al.* [65]. A polycrystalline sample of $Na_2Co_2TeO_6$ was prepared from Na_2CO_3 (Merck, 99.9%), Co_3O_4 (Sigma-Aldrich, 99.99%), and TeO_2 (Sigma-Aldrich, 99.9995%). Following the method described by Berthelot *et al.* [72], the reagents were ground together at the correct stoichiometry, pressed into pellets, and calcined twice at 850°C in air for 12 h with intermediate regrinding. Sample purity was confirmed by x-ray powder diffraction. Magnetic property measurements were also consistent with previous reports for $Na_2Co_2TeO_6$: zero-field-cooled temperature-dependent susceptibility in a 0.1-T field showed a sharp antiferromagnetic transition at $T_N = 27$ K and a weaker feature at 16 K, which were suppressed under field-cooled conditions. A Curie-Weiss fit to the paramagnetic region yielded an effective magnetic moment of 4.02 μ_B/Co (within the range typically observed for Co^{2+}) and a Weiss constant $\theta_{CW} = -1.4$ K.

III. INELASTIC NEUTRON SCATTERING

INS data were collected using the cold-neutron time-of-flight spectrometer Pelican [73,74] at the Australian Centre for Neutron Scattering. Approximately 5 g of each sample was held in an annular sample can

fabricated from oxygen-free copper. This was cooled using a dilution insert inside a top-loading closed cycle cryostat. The instrument was aligned for 4.69 Å neutrons. The choppers were also rephased to allow the collection of data with $\lambda/2 = 2.345$ Å neutrons. Data were collected at 50 mK and 1.8 K and corrected for background by subtraction of an empty can and normalized to a standard vanadium sample. All raw detector data were processed using the freely available LAMP [75] software.

Magnetic Bragg reflections were observed at $Q = 0.75$Å, confirming that the system was indeed magnetically ordered for the measured temperatures. It is common to observe up to three phase transitions in $Na_2Co_2TeO_6$; a well-known transition at ∼26K coinciding with the appearance of zigzag magnetic Bragg peaks [67], a weaker transition at 31 K [76], and the weakest at 14 K [77]. The 14-K transition may be due to a subtle magnetic effect, such as interlayer ordering. Ref. [55] includes a weak interlayer Heisenberg coupling when calculating spin-wave dispersions, from which one may estimate its magnitude at around ∼0.4 meV. We concern ourselves principally with the low-lying excitations of the high-symmetry M point, at which the dynamics are dominated by the SO(3) symmetry breaking terms responsible for opening the gap.

$Na_2Co_2TeO_6$ at 50 mK clearly features a mode emanating from $Q = 0.75$ Å, corresponding to the M point in the Brillouin zone of the honeycomb layers. The dispersion relation close to this point appears to be linear. Our results are consistent with existing experiments [53–55,76], however, our ability to resolve features below 1 meV provides crucial detail at the gap point (i.e., where the magnon excitation gets closest to the elastic line). In fact, we are able to resolve energy transfers down to 0.2 meV [see Figs. 1(a)–1(d)]. The single-Q cuts of the data in Fig. 1(c), shown in Figs. 2(a) and 2(c), exhibit a statistically significant excess of spectral weight down to the elastic line with an essentially linear intensity fall-off. This seemingly gapless spectrum disagrees somewhat with existing models, which are generally gapped by several meV. It it not obvious *a priori* how large of a modification to these models is necessary to fit our experiment.

The spectrum for $Na_3Co_2SbO_6$ shows no evidence of any low-energy modes near the M or K points, the sole resolvable magnon excitation appears to emanate from Γ. The dispersion resembles a quadratic mode, which may be compatible with the magnon spectrum predicted by Ref. [63]. Unlike $Na_2Co_2TeO_6$, there is very little difference between the two temperatures in Figs. 1(d) and 1(f).

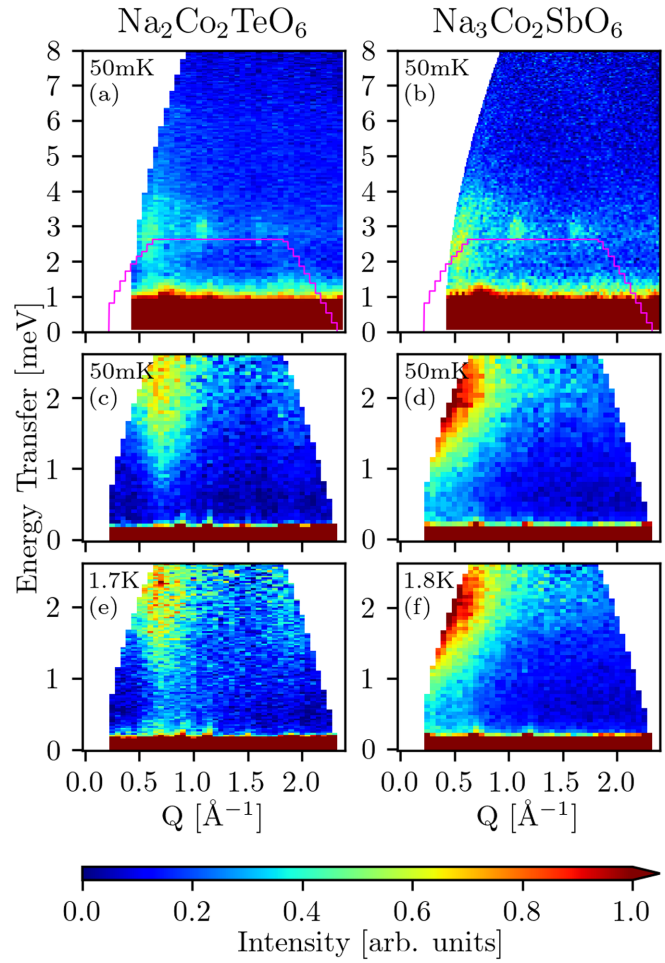

FIG. 1. INS results for powder samples of $Na_2Co_2TeO_6$ (left column) and $Na_3Co_2SbO_6$ (right column). (a)–(d) are measured at $T = 50$ mK while (e) and (f) at 1.7 and 1.8 K, respectively. Detector resolution is 0.135 μeV, 0.01 Å^{-1}. Data gathered at $\lambda/2 = 2.345$ Å are shown in panels (a) and (b), remaining plots were collected at $\lambda = 4.69$ Å. Pink curves on (a) and (b) correspond to domain of intensity data shown in (c), (f).

IV. SPIN-WAVE THEORY

We model the system using a six-parameter extended Heisenberg-Kitaev model as previously used in Refs. [53–55]. The first-order anisotropic interactions are the most general possible couplings that preserve C_3 symmetry, parameterized by J_1, K, Γ, Γ' (explained below). These are supplemented by second and third-nearest neighbor Heisenberg couplings of respective strengths J_2 and J_3. This is motivated by *ab intio* calculations of realistic, distorted octahedral lattices [63] and the failure of simpler models to accurately reproduce analogous systems such as $\alpha-RuCl_3$ and A_2IrO_3 [59] (A=Na or Li). Following the original proposal for the realisation of bond-anisotropic couplings [10], we take the quantisation axes x, y, z to be oriented as in Fig. 3, i.e., normal to the corresponding edge-sharing rectangles. The Hamiltonian may be expressed in the form

$$\begin{aligned}\mathcal{H} = \sum_{\langle ij\rangle^\gamma} \big\{ & J_1 \mathbf{S}_i \cdot \mathbf{S}_j + K S_i^\gamma S_j^\gamma + \Gamma \left(S_i^\alpha S_j^\beta + S_i^\beta S_j^\alpha \right) \\ & + \Gamma' \left(S_i^\gamma S_j^\alpha + S_i^\gamma S_j^\beta + S_i^\alpha S_j^\gamma + S_i^\beta S_j^\gamma \right) \big\} \\ & + J_2 \sum_{\langle\langle ij\rangle\rangle} \mathbf{S}_i \cdot \mathbf{S}_j + J_3 \sum_{\langle\langle\langle ij\rangle\rangle\rangle} \mathbf{S}_i \cdot \mathbf{S}_j . \end{aligned} \tag{1}$$

Here J_i represents ith neighbor isotropic Heisenberg spin exchange, K is nearest-neighbor Kitaev coupling while Γ and Γ′ are symmetric off-diagonal couplings. Indices within single (double and triple) brackets $\langle\cdot\rangle$ denote nearest (second and third nearest) neighbors lattice sites. The notation $\sum_{\langle ij\rangle^\gamma}$ refers to a sum over all nearest neighbour sites, with $\gamma = x, y, z$ chosen according to bond orientation. For each bond

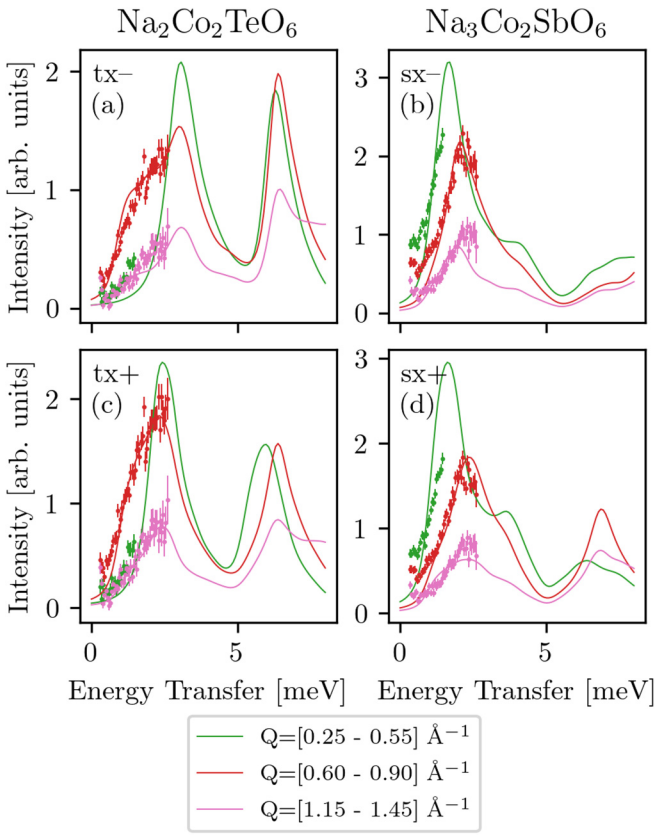

FIG. 2. Best fit of LSWT models to 50 mK INS data of $Na_2Co_2TeO_6$ (tx) and $Na_3Co_2SbO_6$ (sx). The plus/minus sign refers to a model with positive or negative K, respectively (see Table I). Experimental data is shown in points with error bars, theory is shown with smooth curves.

α, β are chosen such that (α, β, γ) is a cyclic permutation of (x, y, z). The first two lines of Eq. (1) may be written more compactly as $\mathcal{H}^{(1)} = \sum_{\langle ij \rangle^\gamma} \mathbf{S}_i^T K_\gamma \mathbf{S}_j$ using the matrices

$$K_x = \begin{pmatrix} K+J & \Gamma' & \Gamma' \\ \Gamma' & J & \Gamma \\ \Gamma' & \Gamma & J \end{pmatrix}, \quad K_y = \begin{pmatrix} J & \Gamma' & \Gamma \\ \Gamma' & K+J & \Gamma' \\ \Gamma & \Gamma' & J \end{pmatrix}, \tag{2}$$

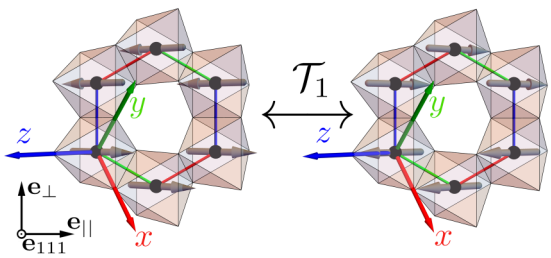

FIG. 3. Classical magnetic moments (gray) of $j = \frac{1}{2}$ pseudospins relative to CoO_8 octahedra (peach). Left and right diagrams show conjugate models under the duality transformation $\mathcal{T}_1$. Red, green, and blue bonds correspond to Kitaev interactions along the x, y, and z axes, respectively. $\mathbf{e}_\parallel$, $\mathbf{e}_\perp$, and $\mathbf{e}_{111}$ are defined in Sec. VI C.

$$K_z = \begin{pmatrix} J & \Gamma & \Gamma' \\ \Gamma & J & \Gamma' \\ \Gamma' & \Gamma' & K+J \end{pmatrix}. \tag{3}$$

The magnetic Bragg peaks observed in both materials of our experiment are consistent with the results of previous work [65–67], which suggest a zig-zag ground state. We employ standard linear spin-wave theory to probe the quantum fluctuations about a polarized classical ground state. The ground state vector is not chosen spontaneously; in general, the anisotropic interactions break SU(2) symmetry fixing the orientation of the magnetic moments relative to the lattice. This optimal ground state is found analytically in Sec. VI C.

About this ground state, we expand in Holstein-Primakoff bosons, from which we deduce the magnon dispersion $\epsilon_i(\mathbf{Q})$ and spectral weight function $S^{\alpha\beta}(\mathbf{Q}, \omega)$. In the linearized approximation, all three-operator terms are discarded and excited states have infinite lifetimes, resulting in $S(\mathbf{Q}, \omega) \propto \sum_{i=1}^{N} S_i(\mathbf{Q}) \delta(\omega - \epsilon_i(\mathbf{Q}))$, where $N = 4$ is the number of magnetic sites per unit cell.

We capture the effects of finite detector resolution and magnon damping by convolving the spectrum with a Voigt profile. The Gaussian standard deviation introduced by the settings of the Pelican spectrometer is 0.135 meV, but the Lorentzian broadening was determined phenomenologically. We fit a slice from the single crystal data of Ref. [76], finding $\gamma = 0.25(5)$ meV to give an acceptable fit to the low-energy peaks (see Appendix). Although the broadening is in general Q dependent, the single crystal evidence seems to suggest that any variation is fairly weak [76].

It has recently been suggested [78] that corrections from many-magnon interactions are essential when fitting frustrated Kitaev-like models to high-energy (>3 meV) magnon spectra. Magnon energy renormalizations and lifetime broadening can be both substantial (of order ∼1 meV) and highly anistropic [79,80], particularly in the presence of large off-diagonal couplings Γ, Γ'. Multi-magnon excited state energies are bounded below by a sharp dispersive cutoff, corresponding to the minimum combined energy of two magnons with $k_1 + k_2 = k$. In a neutron scattering experiment, this manifests as a sharp change in broadening when the decay channel $k \to k_1 + k_2$ becomes kinematically allowed [80]. Known single crystal data for the minimum energy mode [76] shows no such broadening discontinuities, suggesting that the linear approximation is appropriate for the lowest energy mode.

V. FITTING THE POWDER SPECTRUM

For both materials, our long-wavelength neutron experiments have access to the low energy $E < 4$ meV region of Q–E space, at the cost of only seeing low-energy details. As we do not have access to the high-energy features that aided the qualitative fitting of models in Refs. [54] and [53], we require a quantitative goodness-of-fit measure to navigate the five-dimensional (5D) parameter space. We therefore adopt

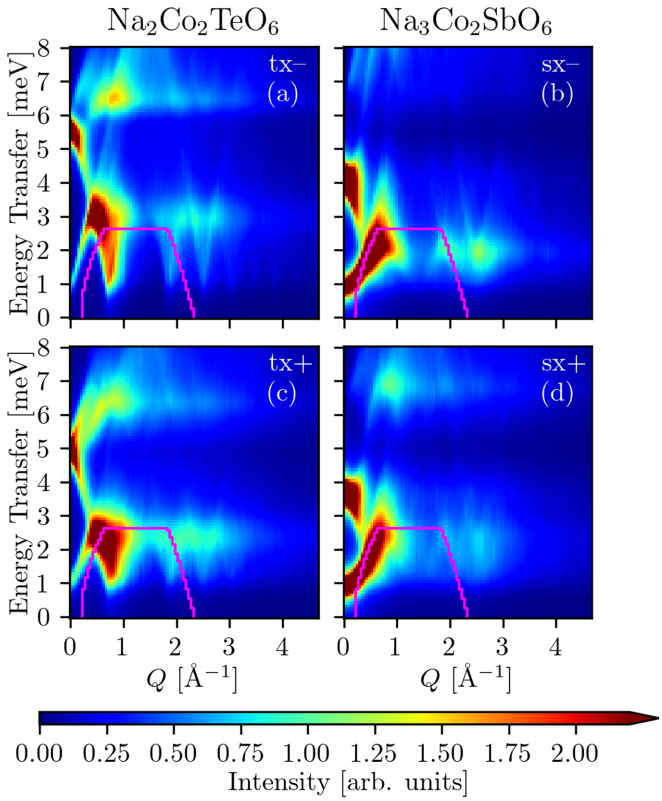

FIG. 4. Calculated powder averages for $Na_2Co_2TeO_6$ (left column) and $Na_3Co_2SbO_6$ (right column).

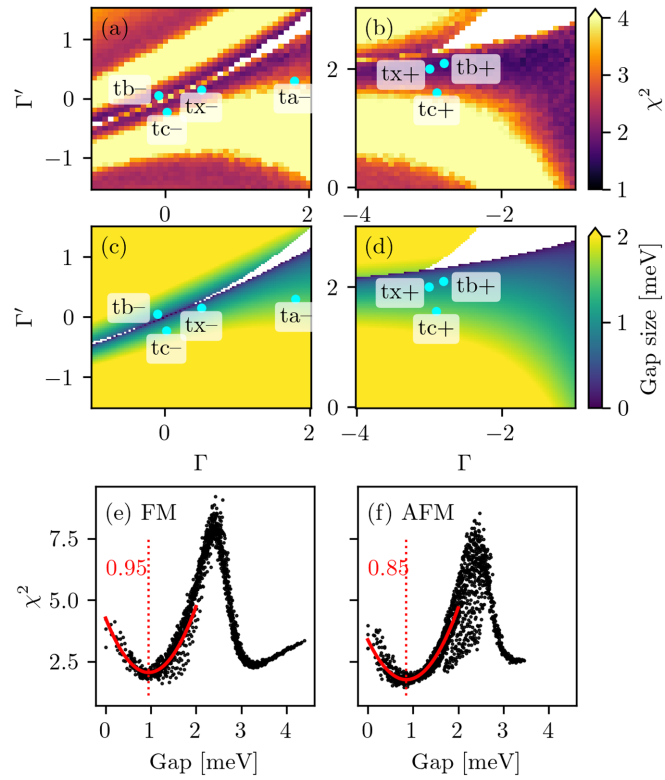

FIG. 5. χ^2 values and gap sizes for perturbations of the tx- (left column) and tx+ (right column) $Na_2Co_2TeO_6$ models in $\Gamma - \Gamma'$ space, both of which are in units of meV. White regions indicate that the Hamiltonian is not positive definite, meaning that the classical magnetic structure is not zig-zag. Pixel size is indicative of grid used for parameter generation. All χ^2 values from (a), (b) are shown against their corresponding gap in (e), (f), with interpolating parabolas as a guide to the eye.

the approach of Ref. [55]. We define

$$\chi^2 = \sum_{Q,\omega} \frac{(\mathcal{I}_{\text{exp}}(Q,\omega) - \mathcal{I}_{\text{theory}}(Q,\omega))^2}{\mathcal{I}_{\text{exp}}(Q,\omega)}, \tag{4}$$

where $\mathcal{I}_{\text{exp}}$ is the experimental scattering intensity and $\mathcal{I}_{\text{theory}}(Q,\omega) \propto F(Q)^2 S^{\perp}(Q,\omega)$. $F(Q)$ is the spherically symmetric atomic form factor of Co^{2+} [81], and $S^{\perp}$ is as defined in Eq. (9). The theoretical intensity function is normalized to have the same total intensity as the experiment, when restricted to pixels within kinematic limits and at an energy above 4 meV. This energy cut was used to exclude the elastic line. All plots shown account for the form factor fall-off of the magnetic Co ions.

Due to the lack of clearly resolved high energy features in our 4.69 Å data on either substance [see Figs. 1(a) and 1(b)], fine detail at low Q provides the most useful information for model fitting. We therefore used the experimental intensity at 50 mK from Figs. 1(c) and 1(d) for $\mathcal{I}_{\text{exp}}$. The domain of the low-energy data is outlined in pink on Fig. 4.

The powder averaging of the inelastic neutron data from the polycrystalline sample makes unique determination of best-fit parameters difficult. Previous reports on these compounds have consistently found weak J_2 when it is included in $Na_2Co_2TeO_6$ [53–55], and all previous fit attempts have neglected it when fitting $Na_3Co_2SbO_6$. Due to the small region of data available, we set $J_2 = 0$ to mitigate overparameterization.

Model parameters were optimized by the following procedure:

(1) Suggest a starting guess for the six parameters.

(2) Compute χ^2 for a rectangle of side 2 meV centered on the guess in $\Gamma - \Gamma'$ space, $J_1 - K$ space and $J_1 - J_3$ space.

(3) Compare the local minima of these three phase portraits, and update the guess to match.

This procedure was successful in obtaining close matches of the binned powder data to the theoretical model. The $Na_2Co_2TeO_6$ models in Figs. 2(a) and 2(c) are close matches with the expeirmental cuts, subject to some slight variations that may be attributed to momentum-space broadening from defects; a factor not accounted for in the theoretical model. In particular, the low-momentum cut between 0.25 Å^{-1} and 0.55 Å^{-1} is likely contaminated by diffraction from the zero-order peak.

The parameters ultimately obtained should not be interpreted as rigorous global minima of the error term. Rather, they should be taken as estimates that reflect the general hierarchy of coupling strengths. It is not possible to assign meaningful error bars to these parameters; as illustrated in Fig. 5, the χ^2 surface is riddled with sharp valleys, flat plateaus, and local minima that are resistant to purely numerical optimization methods. In practice, it was necessary to manually choose a minimum. The parameters are interrelated in a highly nontrivial manner, so any statement about param-

eter confidence must be specified as a manifold embedded in the 5D parameter space. The intersection of the valleys given by our data with the more localized maxima found in Ref. [55], serves to specify the parameter ranges more tightly.

We chose the starting guesses for $Na_2Co_2TeO_6$ using the work of Refs. [55], which established regions of parameter space in agreement with their good quality high energy data. We seek to further restrict the allowed parameter space and use these models to deduce qualitative features of the magnon spectrum, e.g., whether or not it has a gap in the excitation spectrum. No such study exists for $Na_3Co_2SbO_6$, so starting guesses were chosen centered on the sa and sb± best-fit parameters from Refs. [53,54], which are listed in Table I.

VI. DISCUSSION

A. Model duality and sign of *K*

It is known that best fit parameters for the extended Heisenberg-Kitaev-Γ-Γ′ model tend to come in pairs. Looking at $Na_2Co_2TeO_6$, $Na_3Co_2SbO_6$ and the $Na_2Co_2TeO_6$analog $Na_2Ni_2TeO_6$, Refs. [54,55] assigned two models to each compound, one with a dominant $K < 0$ interaction, and one with a more modest antiferromagnetic K of similar magnitude to J_1, Γ and Γ′. We will refer to these model classes as ferromagnetic (FM, –) and antiferromagnetic (AFM, +), respectively. Our work follows the same pattern: the top and bottom rows of Fig. 4 show two ostensibly unrelated models with extremely similar powder averages. This correspondence is due to the exact duality transformation identified by Chaloupka and Khalliulin [31]. The $\mathcal{T}_1$ transformation as defined in their paper rotates spin space by π about the honeycomb plane normal vector $\mathbf{e}_{111}$, which in our xyz spin basis may be expressed as the rotation (5):

$$\mathbf{S}_i \mapsto Z\mathbf{S}_i,$$
$$Z = \begin{pmatrix} -\frac{1}{3} & +\frac{2}{3} & +\frac{2}{3} \\ +\frac{2}{3} & -\frac{1}{3} & +\frac{2}{3} \\ +\frac{2}{3} & +\frac{2}{3} & -\frac{1}{3} \end{pmatrix}. \tag{5}$$

Note that $|Z| = 1, Z = Z^T = Z^{-1}$. By applying this transformation to the K_γ matrices defined in Eqs. (2) and (3), one may easily verify that there exist transformed parameters $\tilde{J}, \tilde{K}, \tilde{\Gamma}, \tilde{\Gamma}'$ such that

$$K_\gamma(\tilde{J}, \tilde{K}, \tilde{\Gamma}, \tilde{\Gamma}') = ZK_\gamma(J, K, \Gamma, \Gamma')Z. \tag{6}$$

This leads to a linear relationship between the original and transformed parameters. Following Ref. [31], we denote this parameter transformation $\mathcal{T}_1$. Its matrix representation is presented in Eq. (7).

$$\begin{pmatrix} \tilde{J} \\ \tilde{K} \\ \tilde{\Gamma} \\ \tilde{\Gamma}' \end{pmatrix} = \begin{pmatrix} 1 & +\frac{4}{9} & -\frac{4}{9} & +\frac{4}{9} \\ 0 & -\frac{1}{3} & +\frac{4}{3} & -\frac{4}{3} \\ 0 & +\frac{4}{9} & +\frac{5}{9} & +\frac{4}{9} \\ 0 & -\frac{2}{9} & +\frac{2}{9} & +\frac{7}{9} \end{pmatrix} \begin{pmatrix} J \\ K \\ \Gamma \\ \Gamma' \end{pmatrix} = \mathcal{T}_1 \begin{pmatrix} J \\ K \\ \Gamma \\ \Gamma' \end{pmatrix}. \tag{7}$$

Similarly, $Z^2 = \mathbb{1}$ implies that any purely isotropic couplings remain fixed under $\mathcal{T}_1$, i.e., $\tilde{J}_i = J_i$ $(i = 2, 3)$. In the absence of K, Γ, Γ', J_1 would also be fixed.

TABLE II. Dual pairings of best fit parameters.

Model	J	K	Γ	Γ′	J_3
tx–	−0.20	−7.00	0.50	0.15	1.40
$\mathcal{T}_1$(tx+)	0.14	−7.73	0.87	0.18	1.60
tx+	−3.50	3.20	−3.00	2.00	1.60
$\mathcal{T}_1$(tx–)	−3.47	2.80	−2.75	1.78	1.40
sx–	−1.40	−10.00	−0.30	−0.60	0.60
$\mathcal{T}_1$(sx+)	−2.20	−6.40	−1.17	−1.10	0.60
sx+	−5.00	2.00	−4.00	0.30	0.60
$\mathcal{T}_1$(sx–)	−5.98	3.73	−4.94	1.69	0.60

This symmetry implies that two models possessing $\mathcal{T}_1$-equivalent parameters will have indistinguishable magnon excitation spectra. Further, any choice of classical zigzag state is site-wise symmetric under a global π rotation about $\mathbf{e}_{111}$. This symmetry renders the neutron scattering cross section (8) invariant under $\mathcal{S}^{\alpha\beta} \mapsto Z^{\alpha\alpha'}Z^{\beta\beta'}\mathcal{S}^{\alpha'\beta'}$, implying that the two models are fundamentally indistinguishable by scattering experiments that couple only to the spins. The INS cross section is given by

$$\frac{d^2\sigma}{d\Omega dE_f} \propto F(Q)^2 S^\perp(\mathbf{Q}, \omega) \tag{8}$$

with the dynamical structure factor

$$S^\perp(\mathbf{Q}, \omega) = \sum_{\alpha\beta} \left(\delta_{\alpha\beta} - \frac{Q^\alpha Q^\beta}{Q^2}\right) \mathcal{S}^{\alpha\beta}(\mathbf{Q}, \omega) \tag{9}$$

and its matrix elements

$$\mathcal{S}^{\alpha\beta}(\mathbf{Q}, \omega) = \sum_{ij} \int \frac{d\tau}{2\pi} e^{-i\omega\tau} \left\langle S^\alpha_{-\mathbf{Q}i}(0) S^\beta_{\mathbf{Q}j}(\tau) \right\rangle. \tag{10}$$

The powder structure factor is obtained by averaging over all momentum transfer directions:

$$\int d\Omega \frac{d^2\sigma}{d\Omega dE_f} \propto F(Q)^2 \int d\Omega S^\perp(\mathbf{Q}, \omega). \tag{11}$$

The four inequivalent sites in the zig-zag ground state's magnetic unit cell are indexed by i, j, $F(Q)$ is a spherically symmetric atomic scattering factor, and $S^\alpha_{\mathbf{Q}j}(\tau)$ is a Fourier mode of a Heisenberg picture spin operator. We neglect the Debye-Waller factor due to the low temperature.

The symmetry pertains to the spin model, not the linearised spin wave approximation. The two parameter sets are therefore *functionally* indistinguishable; the antiferromagnetic (+) parameter sets, which would seem to have their weak K parameters suppressed by large $J_{1,2,3}$, Γ, Γ′ terms, have equivalent excitation spectra to models with dominant $K < 0$. Note that there are *two* axes in J_1, K, Γ, Γ' space corresponding to pure Kitaev models: the obvious $(0, K, 0, 0)$ axis, and the axis generated by $\mathcal{T}_1(0, K, 0, 0) = K(\frac{4}{9}, -\frac{1}{3}, \frac{4}{9}, -\frac{2}{9})$ for any $K \neq 0$. In general, when off-diagonal contributions are sufficiently small a large $K < 0$ parameter is mapped to a mixture of K, Γ, Γ' with K taking the opposite sign. Table II confirms that this is essentially the case with our model pairs, and indeed the visualization in Fig. 6 confirms that the same is true of most other published models.

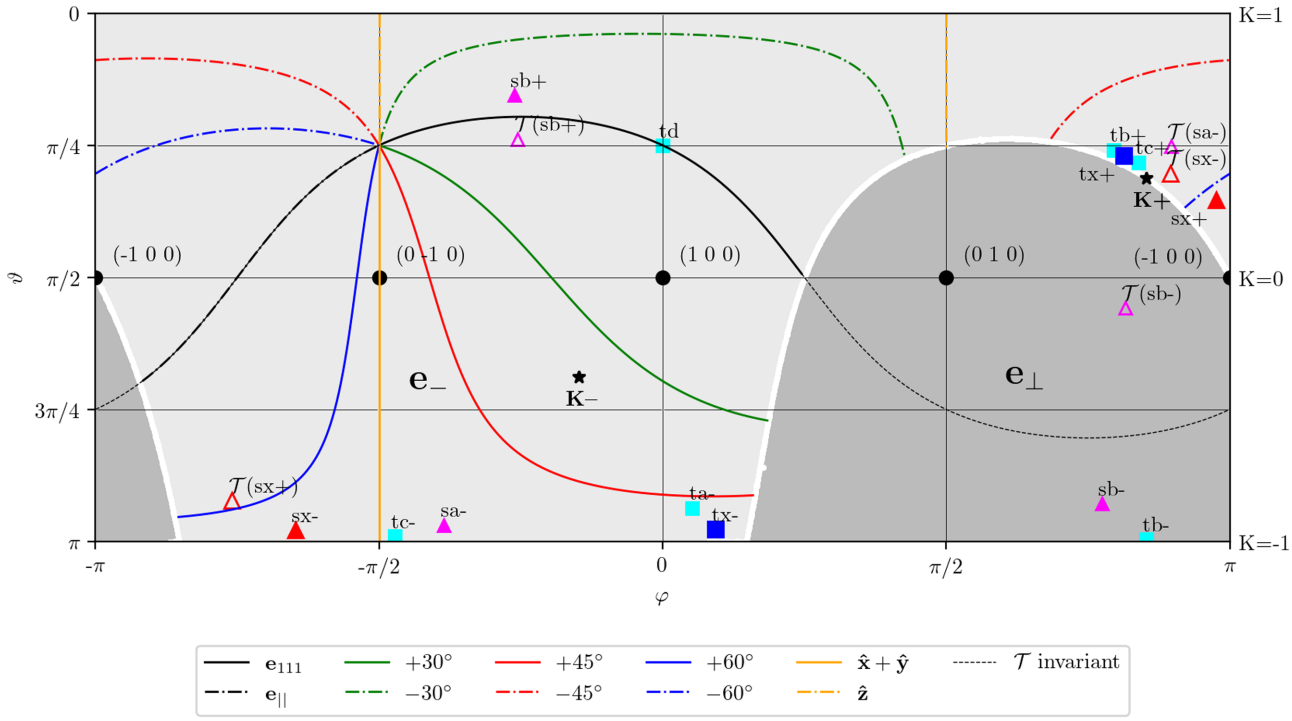

FIG. 6. Ground-state zig-zag magnetic moment orientations over the sphere $\Gamma^2 + (\Gamma')^2 + K^2 = 1$ in (Γ, Γ', K) space, assuming zigzag ground state stability. The sphere is parameterised using $\Gamma = \sin(\vartheta)\cos(\varphi)$, $\Gamma' = \sin(\vartheta)\sin(\varphi)$, $K = \cos(\vartheta)$. In the $\mathbf{e}_-$ phase, meridians are labeled by the angle of $\mathbf{e}_-$ to $\mathbf{e}_{111}$. The fine black dotted line is the intersection of the $\mathcal{T}_1$-invariant plane $K - \Gamma + \Gamma' = 0$ with the unit sphere. **K+** and **K–** indicate the nontrivial hidden Kitaev points [31] generated by $\mathbf{K}\pm = \mathcal{T}_1(0, 0, \mp 1)$. Models are defined in Table I.

Arguably, this makes both parameter sets equally close to a Kitaev spin liquid. All models presented in Table I (with the notable exceptions of td and sb+) either have dominant $K < 0$, or are $\mathcal{T}_1$ equivalent to a model with dominant K, i.e., close to the Kitaev point **K**– (Fig. 6), which is discussed further below. $Na_3Co_2SbO_6$ and $Na_2Co_2TeO_6$ are therefore good candidate materials for field-revealed or strain-revealed quantum spin liquids.

The Hubbard models studied in Refs. [62–64] indicate a robustly ferromagnetic Kitaev interaction over a wide range of parameters. The AFM models arguably all suffer from fine tuning in the Γ, Γ' parameters; a change of only a few percent in either parameter opens the gap to many meV. The FM models correspond to a small trigonal-field perturbation of an ideal edge-sharing geometry, and so would seem to be the more likely explanations of scattering in $Na_2Co_2TeO_6$ and $Na_3Co_2SbO_6$.

B. Existence of a gap

Powder spectra from $Na_2Co_2TeO_6$ [Figs. 1(a), 1(c) and 1(e)] exhibit a clear spin-wave mode emanating from $Q = 0.75$ Å^{-1}, corresponding to the M point of the in-plane Brillouin zone. Our data show a weak spectral weight extending all the way down to the elastic line, which may, in principle, be evidence of a gapless magnon excitation. However, our best-fit results agree with other papers that the spectrum is gapped, though we revise the size of this gap down to 1 meV ± 0.3 meV.

Our model's M point gap is controlled primarily by the parameters Γ and Γ'. As can be seen in Figs. 5(a) and 5(b), the goodness of fit has a W-shaped valley on either side of the gapless line. Crucially, the truly gapless models correspond to a local maximum while the best fit values of Γ, Γ' for all published models listed here have gaps of order 1 meV. The plot of χ^2 against gap size [Figs. 5(e) and 5(f)] shows a very clear minimum near 0.9 meV. One may heuristically assign an uncertainty of 0.3 meV based on the spread of gap sizes with comparable goodness of fit.

We take this to be strong evidence that $Na_2Co_2TeO_6$ has a gapped spin-wave spectrum. We attribute the weak excess of spectral weight below 1 meV in the low temperature data [Fig. 1(c)] to energy broadening from magnon decoherence. The material's powder averaged magnon spectrum therefore bears a very close resemblance to that of α-$RuCl_3$ at zero magnetic field [41,82].

The 50-mK powder spectrum of $Na_3Co_2SbO_6$ [Figs. 1(b) and 1(d)] tells a different story. There is no evidence of a spin-wave mode emanating from the M point, all spectral weight is concentrated near a broad feature at the Γ point. Both best-fit models concur that the mode is quadratic with a gap of order ∼1 meV, as can be seen in the powder averaged theory predictions [Figs. 4(b) and 4(d)]. A more precise bound is not possible due to the occlusion of the Γ point by the zero-order neutron peak.

Figure 1(e) shows the appearance of an unexpected hourglass feature when the temperature is increased from 50 mK. Data for 50 mK, 1.7 K and 7.4 K along with constant energy

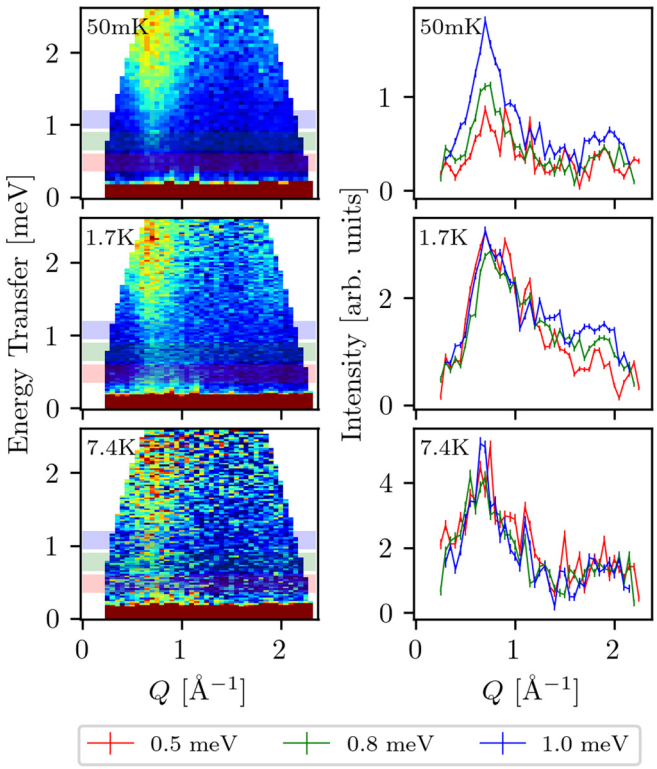

FIG. 7. Constant energy slices of $Na_2Co_2TeO_6$ for $T = 0.05$ K (top row), $T = 1.7$ K (middle row) and $T = 7.4$ K (bottom row) revealing temperature dependence of the M point (0.7 Å^{-1}) signal.

cuts is shown in Fig. 7. The excitation near zero energy is very broad in Q, and has a clearly observable waist that excludes the possibility that it is the result of magnon lifetime broadening (see the finite-temperature modeling of α-$RuCl_3$ modelled in Refs. [78–80]). The feature we see is shadowed by elastic scattering in many experiments [53,55], but is arguably visible (albeit in low resolution) in Fig. 5 of Ref. [54], taken at 3 K. The feature is not readily discernible in the single-crystal data of Ref. [76], also at 3 K.

Though it is tempting to draw comparisons with the hourglass magnetic excitations of copper oxide superconductor relatives [83,84], it is more likely that the signal we observe arises from broadening of the magnetic Bragg peak in energy-momentum space, which is consistent with a finite average domain size [85].

While we cannot conclusively explain the hourglass feature, we would like to emphasize that only due to the high resolution of our data, allowing us to access energy transfers below 0.5 meV, it is possible at all to resolve it. In Refs. [53,55] the elastic line is at higher energies than 0.5 meV and the hourglass feature, if it was present, would be hidden (as mentioned above, perhaps it is visible in Fig. 5 of Ref. [54]). In contrast, Ref. [68] features data measured at $T = 3$ K with a resolution at low energies, which would allow us to resolve the hourglass feature. However, there is no hourglass feature visible in Fig. 5 of Ref. [68]. The discrepancy between Ref. [68] and our data is due to the different plotting schemes used: if we plot the color scheme of Fig. 1(e) on a linear scale, the figure becomes very similar to Fig. 5(d) of Ref. [68], and the hourglass has disappeared. We thus conclude that our data is likely of similar quality than that of Ref. [68]. We further speculate that it might be that the hourglass feature has also been observed by other experiments.

C. Classical ground state

We make the ansatz that the material is in a colinear zig-zag phase, featuring ferromagnetic chains oriented normal to the z-bond direction. The classical magnetic ground state vector corresponds to the eigenvector of the matrix $M := K_x + K_y - K_z$ of smallest eigenvalue [54]. The Heisenberg interactions shift all eigenvalues uniformly, with no effect on the eigenvector: the eigenvalues and eigenvectors depend only on K, Γ, and Γ', with the explicit forms [54]:

$$\mathbf{e}_\perp \propto (-1, 1, 0),$$
$$\mathbf{e}_\pm \propto (2x - 1 \pm \zeta, \quad 2x - 1 \pm \zeta, 4)(\Gamma \neq 0),$$
$$\lambda_\perp = \Gamma + K - 2\Gamma',$$
$$\lambda_\pm = (2\Gamma' - \Gamma \pm |\Gamma\zeta|)/2.$$

It is convenient to define $\mathbf{e}_\pm$ by analytic continuation when $\Gamma = 0$, excepting the pure-Kitaev special cases which correspond to a triple degenerate hidden SO(3) symmetry. For convenience, we also define the basis vectors from Fig. 3,

$$\mathbf{e}_\parallel = \frac{1}{\sqrt{6}}(1, 1, -2),$$
$$\mathbf{e}_{111} = \frac{1}{\sqrt{3}}(1, 1, 1).$$

We have set $\zeta = \mathrm{sgn}(\Gamma)\sqrt{8 + (2x-1)^2}$ and $x = (K + \Gamma')/\Gamma$. Note that $\lambda_+ > \lambda_-$. When $x = 1$, $\mathbf{e}_\pm$ are aligned with $\mathbf{e}_\parallel$ and $\mathbf{e}_{111}$. Changes in x rotate this orthogonal eigenbasis about $\mathbf{e}_\perp$. The signed rotation angles for various Γ, Γ', K are shown superimposed on Fig. 6.

Given that a minimal eigenvector remains a minimal eigenvector under the uniform rescaling $M \mapsto \alpha M$, $\alpha \in \mathbb{R}_{>0}$, i.e., the zig-zag orientation is not sensitive to the overall energy scale, it is possible to represent all possible spin alignments of zig-zag ground states by looking at the unit sphere in $\Gamma - \Gamma' - K$ space. The action of $\mathcal{T}_1$ on the theory space can be visualized as mirroring about the plane $K + \Gamma' = \Gamma$. On this plane, the spin orientations must be one of $\mathbf{e}_{111}$, $\mathbf{e}_{||}$ and $\mathbf{e}_\perp$, which are clearly eigenvectors of Z with eigenvalues $1, -1$, and -1 respectively.

Crucially, the two pure Kitaev points at the north and south poles are inequivalent. This is true even for a classical spin model; $K = -1$ is a degeneracy point between $\mathbf{e}_-$ and $\mathbf{e}_\perp$, $K = 1$ is deep in the $\mathbf{e}_-$ region. Under $\mathcal{T}_1$ they are mapped not to each other but to other points in parameter space, marked $\mathbf{K}\pm$, which we call hidden Kitaev points. The cluster of AFM $Na_2Co_2TeO_6$ models near $\mathbf{K}-$ is (approximately) mapped to the cluster near the $K = -1$ pole and vice verse, as are the sx$\pm$ models (see Fig. 6).

Representation-theoretic analyses of x-ray and neutron diffraction data suggest that the spins in $Na_2Co_2TeO_6$ are aligned close to $\mathbf{e}_\parallel$ [66,67], with angular uncertainty of order $\sim 30^\circ$. The $Na_2Co_2TeO_6$ models are only slightly beyond this

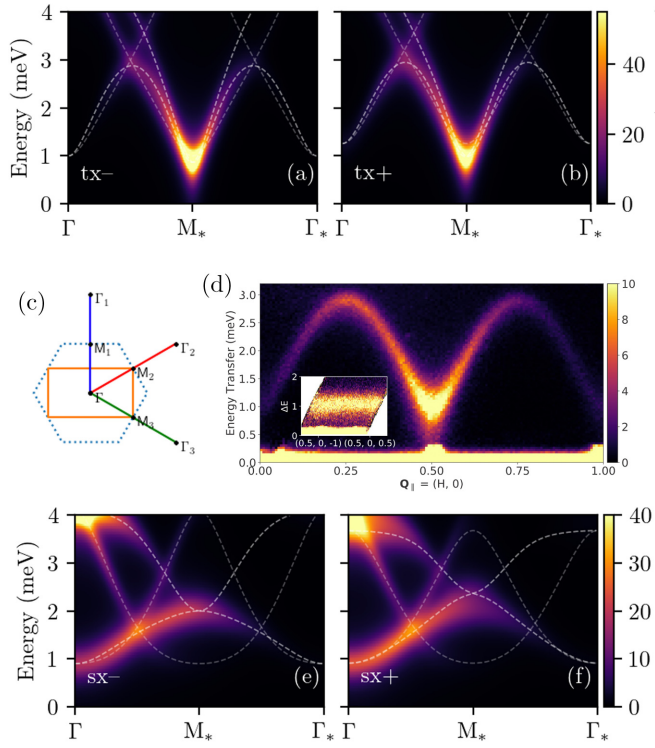

FIG. 8. Domain average over the three Brillouin zone walks (red, green, blue) sketched in (c) for (a) FM and (b) AFM models of $Na_2Co_2TeO_6$. The white dashed lines correspond to the LSWT dispersion relation. (d) Single crystal experimental $Na_2Co_2TeO_6$ data from Ref. [76] for comparison. (e), (f) show analogous plots to (a), (b) for $Na_3Co_2SbO_6$. Linear magnon dispersions are shown in white. $\boldsymbol{Q}_{||} = (0, 0)$ corresponds to the Γ point, and $\boldsymbol{Q}_{||} = (1, 0)$ to Γ′ and the strong accumulation of spectral weight thus appears at M.

uncertainty. It should be emphasized that since these models are found near the critical triple-degenerate Kitaev point at $(0, 0, -1)$ in the (Γ, Γ', K) basis, quantum fluctuations are expected to be large, and higher order magnon interactions may tune the effective zig-zag direction as seen by elastic scattering. For tx–, the classical energy difference between the $\mathbf{e}_\perp$ and $\mathbf{e}_-$ phase is of order $\delta E = 0.4$ meV. Working so close to a classical degeneracy, it is to be expected that the classical ground state calculation will be somewhat inaccurate. The established cluster of models ta–, tb±, tc± are therefore loosely compatible with the reported structure. We note in passing that the anomalous td model from Ref. [54] is a special case, occurring on the nodal $\mathcal{T}$ invariant line with a ground state along $\mathbf{e}_{111}$, which is in tension with the experimentally ascertained magnetic order.

D. Prediction of single crystal results

Figure 8 shows a comparison between domain averages of the $Na_2Co_2TeO_6$ models tx+ and tx– and the single crystal data of Ref. [76]. A single crystal will in general consist of a statistical population of three C_3 related domains corresponding to x, y and z zig-zags. An experiment will therefore detect an average over the three k space paths shown in Fig. 8(c). The paths $\Gamma \to \Gamma_2$ and $\Gamma \to \Gamma_3$ are equivalent under the D_2 symmetry of the Brillouin zone, implying that an experiment should always detect an even number of modes. However, this is not seen in the experimental data, leading the authors of Ref. [76] to suggest that $Na_2Co_2TeO_6$ undergoes a spontaneous charge transfer that renders 1/4 Co sites spinless, leaving the remainder to follows a vortexlike triple-Q order. However, our calculations in Figs. 8(a) and 8(b) show that magnon modes arising from an ensemble of zig-zag orders are equally capable of reproducing the dispersion in Fig. 8(d). Each domain contributes two low-energy magnon modes, resulting in four inequivalent modes. Notably, the doubled modes are the sinusoidlike objects matching the experiment. The missing modes are suppressed by the spin orientation, leading to vanishing spectral weight. While the overall agreement between the single crystal data of Ref. [76] and our theory modeling fitted to our powder sample is surprisingly good, the theoretical prediction is not an exact match. The regions $Q_\parallel < 0.25$, $Q_\parallel > 0.75$ appear too weak in the theoretical prediction, while the crossover at $Q_\parallel = 0.25$ is absent in the experiment. The calculations here are done in the linear approximation, so slight deviations when far from the vacuum are expected. In particular, the modes near high density of states at the M point and the crossover would be expected to have stronger magnon damping, suppressing their INS signals.

The predicted single-crystal scattering signals for the sx– and sx+ $Na_3Co_2SbO_6$ models in Figs. 8(e) and 8(f) are more easily distinguished from each other than the tx± models. This is a consequence of the lack of distinguishing features in the $Na_3Co_2SbO_6$ powder spectrum, which in turn hinders the accurate determination of best-fit parameters. The dispersion ranges over an energy scale of several meV well above the elastic line, with substantial spectral weight away from the Γ point. It is therefore feasible that these features may be observed in a future single crystal experiment on $Na_3Co_2SbO_6$.

VII. CONCLUSION

In this paper we have presented results from INS for $Na_3Co_2SbO_6$ and $Na_2Co_2TeO_6$ measured down to 50 mK. Analysis of the data and comparison with our theoretical modeling shows that spin waves arising from a zig-zag ground state of an extended Heisenberg-Kitaev model are capable of representing the INS behavior of $Na_2Co_2TeO_6$ and $Na_3Co_2SbO_6$. The fine detail that our experiment provides of the M-point excitations of $Na_2Co_2TeO_6$ has allowed us to refine the existing cluster of parameters.

The failure of naive Heisenberg and XXZ models to recreate the magnon dispersions of these materials [53] should be taken as strong evidence of the importance of anisotropic spin couplings. In particular, our $Na_3Co_2SbO_6$ data show a gapped spectrum with no evidence of linear modes emanating from the M point, which is suggestive of substantial SO(3) symmetry breaking.

We have searched for antiferromagnetic and ferromagnetic best-fit models of $Na_2Co_2TeO_6$ and $Na_3Co_2SbO_6$, and demonstrated that they are mapped to each other under the exact duality transformation $\mathcal{T}_1$ of Ref. [31]. This gives us confidence that our model fitting procedure has converged to a global minimum, or at least as close to it as experimental resolution allows.

Fine detail of the M point of $Na_2Co_2TeO_6$ gives strong evidence for the existence of a small gap, which we conservatively estimate to be 1.0(5) meV. This gap is consistent with the dispersion measured by the single-crystal experiment of Ref. [76], and the parameters obtained are close to the existing cluster.

Our $Na_3Co_2SbO_6$ data show an energy minimum at the Γ point, however practical constraints prevent the direct observation of the $Q = 0$ gap. Our use of 4.69 Å neutrons has given us fine detail as close as reasonably practicable to the Γ point, and our best fit extrapolations remain consistent with a broad, quadratic mode. This implies substantial non-spontaneous breaking of SU(2) spin symmetry, however the lack of clearly resolvable features in the spectrum means that we cannot categorically exclude models other than the work presented here. The calculations in Figs. 8(e) and 8(f) show that the predicted magnon dispersion along the $\Gamma \rightarrow \Gamma_*$ line is clearly observable in a single crystal INS experiment.

Our models of both substances (Table II) emphasise the dominance of K over other parameters, suggesting that these materials are very close to the Kitaev spin liquid phase. This would validate the *ab initio* arguments about the nature of $3d^7$ materials as opposed to the d^5 metals Ir and Ru that have dominated searches in the past decade [16,41,56,86], specifically that the tighter orbital confinement suppresses the direct Co-Co exchange responsible for Heisenberg interactions [59,62,69]. These models are consistent with *ab initio* calculations, which unambiguously show that cobaltate honeycombs have a ferromagnetic K. We consider the AFM models to be the less likely set of parameters – they have substantial off-diagonal couplings, corresponding to large trigonal distortions of the honeycomb lattice, and are in some sense fine tuned.

Current INS experimental data cannot distinguish between AFM and FM models linked by $\mathcal{T}_1$ duality. This ambiguity has recently been conclusively resolved in α-$RuCl_3$ by the use of resonant elastic x-ray scattering on a high-quality single crystal [50]. In principle, INS with a symmetry breaking in-plane magnetic field might be an alternative strategy to distinguish the two.

Our best fit models of $Na_2Co_2TeO_6$ and $Na_3Co_2SbO_6$ seem to suggest that the substitution of tellurium by antimony only marginally affects the spin exchange physics. Recent experiments have observed that zig-zag order breaks down for $Na_2Co_2TeO_6$ at large magnetic fields, potentially entering a spin-liquid state [68,87]. To the authors' best knowledge, $Na_3Co_2SbO_6$ has not been probed with a magnetic field to date. Our results suggest the cross-hexamer J_3 coupling, largely responsible for stabilising the zig-zag state, may be weaker in $Na_3Co_2SbO_6$, suggesting a possibly lower critical magnetic field. We therefore suggest that our work be read as further motivation for the study of $Na_3Co_2SbO_6$ as a field-revealed Kitaev QSL candidate.

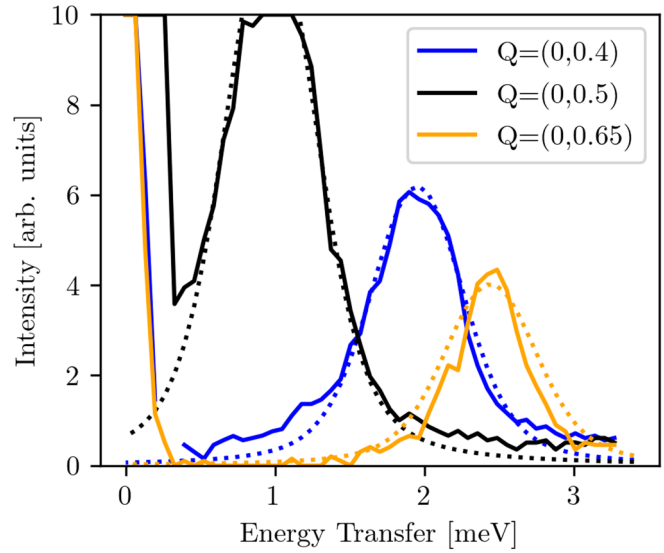

FIG. 9. Empirical fit of slices from single crystal data in [76] by Voigt functions, each with $\gamma = 0.25$ meV and $\sigma = 0.135$ meV. Note that the M point feature (notated here as $Q = (0, 0.5)$ reciprocal lattice units) shows the strongest broadening, while the higher energy features are sharper.

ACKNOWLEDGMENTS

The authors acknowledge discussions with M. Vojta, L. Janssen, I. I. Mazin, and H. O. Jeschke. S.R. and C.D.L. acknowledge support from the Australian Research Council through Grants No. FT180100211 and No. DP200100959, respectively. We also acknowledge the provision of beamtime (under proposal P7327) by the Australian Centre for Neutron Scattering and support from the sample environment team.

APPENDIX: DETAILS OF $Na_2Co_2TeO_6$ BROADENING FUNCTION DETERMINATION

We determined the Lorentzian lifetime broadening phenomenologically, by performing a Voigt profile fit to the available single crystal data. The empirical fits are shown in Fig. 9.

[1] P. Anderson, Resonating valence bonds: A new kind of insulator? Mater. Res. Bull. **8**, 153 (1973).
[2] P. Fazekas and P. W. Anderson, On the ground state properties of the anisotropic triangular antiferromagnet, Philos. Mag.: J. Theor. Exp. Appl. Phys **30**, 423 (1974).
[3] L. Balents, Spin liquids in frustrated magnets, Nature (London) **464**, 199 (2010).
[4] L. Savary and L. Balents, Quantum spin liquids: A review, Rep. Prog. Phys. **80**, 016502 (2017).
[5] Y. Zhou, K. Kanoda, and T.-K. Ng, Quantum spin liquid states, Rev. Mod. Phys. **89**, 025003 (2017).
[6] J. S. Helton, K. Matan, M. P. Shores, E. A. Nytko, B. M. Bartlett, Y. Yoshida, Y. Takano, A. Suslov, Y. Qiu, J.-H. Chung, D. G. Nocera, and Y. S. Lee, Spin Dynamics of the Spin-1/2

Kagome Lattice Antiferromagnet $ZnCu_3(OH)_6Cl_2$, Phys. Rev. Lett. **98**, 107204 (2007).

[7] T.-H. Han, J. S. Helton, S. Chu, D. G. Nocera, J. A. Rodriguez-Rivera, C. Broholm, and Y. S. Lee, Fractionalized excitations in the spin-liquid state of a kagome-lattice antiferromagnet, Nature (London) **492**, 406 (2012).

[8] B. J. Powell and R. H. McKenzie, Quantum frustration in organic Mott insulators: From spin liquids to unconventional superconductors, Rep. Prog. Phys. **74**, 056501 (2011).

[9] A. Y. Kitaev, Anyons in an exactly solved model and beyond, Ann. Phys. **321**, 2 (2006).

[10] G. Jackeli and G. Khaliullin, Mott Insulators in the Strong Spin-Orbit Coupling Limit: From Heisenberg to a Quantum Compass and Kitaev Models, Phys. Rev. Lett. **102**, 017205 (2009).

[11] G. Khaliullin, Orbital order and fluctuations in Mott insulators, Prog. Theor. Phys. Suppl. **160**, 155 (2005).

[12] T. Takayama, J. Chaloupka, A. Smerald, G. Khaliullin, and H. Takagi, Spin–orbit-entangled electronic phases in 4*d* and 5*d* transition-metal compounds, J. Phys. Soc. Jpn. **90**, 062001 (2021).

[13] Y. Singh and P. Gegenwart, Antiferromagnetic Mott insulating state in single crystals of the honeycomb lattice material Na_2IrO_3, Phys. Rev. B **82**, 064412 (2010).

[14] X. Liu, T. Berlijn, W.-G. Yin, W. Ku, A. Tsvelik, Y.-J. Kim, H. Gretarsson, Y. Singh, P. Gegenwart, and J. P. Hill, Long-range magnetic ordering in Na_2IrO_3, Phys. Rev. B **83**, 220403(R) (2011).

[15] Y. Singh, S. Manni, J. Reuther, T. Berlijn, R. Thomale, W. Ku, S. Trebst, and P. Gegenwart, Relevance of the Heisenberg-Kitaev Model for the Honeycomb Lattice Iridates A_2IrO_3, Phys. Rev. Lett. **108**, 127203 (2012).

[16] S. K. Choi, R. Coldea, A. N. Kolmogorov, T. Lancaster, I. I. Mazin, S. J. Blundell, P. G. Radaelli, Y. Singh, P. Gegenwart, K. R. Choi, S.-W. Cheong, P. J. Baker, C. Stock, and J. Taylor, Spin Waves and Revised Crystal Structure of Honeycomb Iridate Na_2IrO_3, Phys. Rev. Lett. **108**, 127204 (2012).

[17] F. Ye, S. Chi, H. Cao, B. C. Chakoumakos, J. A. Fernandez-Baca, R. Custelcean, T. F. Qi, O. B. Korneta, and G. Cao, Direct evidence of a zigzag spin-chain structure in the honeycomb lattice: A neutron and x-ray diffraction investigation of single-crystal Na_2IrO_3, Phys. Rev. B **85**, 180403(R) (2012).

[18] I. I. Mazin, H. O. Jeschke, K. Foyevtsova, R. Valentí, and D. I. Khomskii, Na_2IrO_3 as a Molecular Orbital Crystal, Phys. Rev. Lett. **109**, 197201 (2012).

[19] C. C. Price and N. B. Perkins, Critical Properties of the Kitaev-Heisenberg Model, Phys. Rev. Lett. **109**, 187201 (2012).

[20] R. Comin, G. Levy, B. Ludbrook, Z.-H. Zhu, C. N. Veenstra, J. A. Rosen, Y. Singh, P. Gegenwart, D. Stricker, J. N. Hancock, D. van der Marel, I. S. Elfimov, and A. Damascelli, Na_2IrO_3 as a Novel Relativistic Mott Insulator with a 340-meV Gap, Phys. Rev. Lett. **109**, 266406 (2012).

[21] J. Reuther, R. Thomale, and S. Rachel, Magnetic ordering phenomena of interacting quantum spin Hall models, Phys. Rev. B **86**, 155127 (2012).

[22] H. Gretarsson, J. P. Clancy, X. Liu, J. P. Hill, E. Bozin, Y. Singh, S. Manni, P. Gegenwart, J. Kim, A. H. Said, D. Casa, T. Gog, M. H. Upton, H.-S. Kim, J. Yu, V. M. Katukuri, L. Hozoi, J. van den Brink, and Y.-J. Kim, Crystal-Field Splitting and Correlation Effect on the Electronic Structure of A_2IrO_3, Phys. Rev. Lett. **110**, 076402 (2013).

[23] H. Gretarsson, J. P. Clancy, Y. Singh, P. Gegenwart, J. P. Hill, J. Kim, M. H. Upton, A. H. Said, D. Casa, T. Gog, and Y.-J. Kim, Magnetic excitation spectrum of Na_2IrO_3 probed with resonant inelastic x-ray scattering, Phys. Rev. B **87**, 220407(R) (2013).

[24] K. Foyevtsova, H. O. Jeschke, I. I. Mazin, D. I. Khomskii, and R. Valentí, Ab initio analysis of the tight-binding parameters and magnetic interactions in Na_2IrO_3, Phys. Rev. B **88**, 035107 (2013).

[25] J. Reuther, R. Thomale, and S. Rachel, Spiral order in the honeycomb iridate Li_2IrO_3, Phys. Rev. B **90**, 100405(R) (2014).

[26] B. H. Kim, G. Khaliullin, and B. I. Min, Electronic excitations in the edge-shared relativistic mott insulator: Na_2IrO_3, Phys. Rev. B **89**, 081109(R) (2014).

[27] J. G. Rau, E. K.-H. Lee, and H.-Y. Kee, Generic Spin Model for the Honeycomb Iridates beyond the Kitaev Limit, Phys. Rev. Lett. **112**, 077204 (2014).

[28] S. Hwan Chun, J.-W. Kim, J. Kim, H. Zheng, C. C. Stoumpos, C. D. Malliakas, J. F. Mitchell, K. Mehlawat, Y. Singh, Y. Choi, T. Gog, A. Al-Zein, M. M. Sala, M. Krisch, J. Chaloupka, G. Jackeli, G. Khaliullin, and B. J. Kim, Direct evidence for dominant bond-directional interactions in a honeycomb lattice iridate Na_2IrO_3, Nat. Phys. **11**, 462 (2015).

[29] I. Kimchi, R. Coldea, and A. Vishwanath, Unified theory of spiral magnetism in the harmonic-honeycomb iridates α, β, and γ-Li_2IrO_3, Phys. Rev. B **91**, 245134 (2015).

[30] Y. Li, K. Foyevtsova, H. O. Jeschke, and R. Valentí, Analysis of the optical conductivity for $A_2IrO_3 (A = \mathrm{Na}, \mathrm{Li})$ from first principles, Phys. Rev. B **91**, 161101(R) (2015).

[31] J. Chaloupka and G. Khaliullin, Hidden symmetries of the extended Kitaev-Heisenberg model: Implications for the honeycomb-lattice iridates A_2IrO_3, Phys. Rev. B **92**, 024413 (2015).

[32] I. Rousochatzakis, J. Reuther, R. Thomale, S. Rachel, and N. B. Perkins, Phase Diagram and Quantum Order by Disorder in the Kitaev $K_1 - K_2$ Honeycomb Magnet, Phys. Rev. X **5**, 041035 (2015).

[33] S. Nishimoto, V. M. Katukuri, V. Yushankhai, H. Stoll, U. K. Rössler, L. Hozoi, I. Rousochatzakis, and J. van den Brink, Strongly frustrated triangular spin lattice emerging from triplet dimer formation in honeycomb Li_2IrO_3, Nat. Commun. **7**, 10273 (2016).

[34] A. Catuneanu, H.-S. Kim, O. Can, and H.-Y. Kee, Topological edge states in correlated honeycomb materials with strong spin-orbit coupling, Phys. Rev. B **94**, 121118(R) (2016).

[35] S. C. Williams, R. D. Johnson, F. Freund, S. Choi, A. Jesche, I. Kimchi, S. Manni, A. Bombardi, P. Manuel, P. Gegenwart, and R. Coldea, Incommensurate counterrotating magnetic order stabilized by Kitaev interactions in the layered honeycomb $\alpha-Li_2IrO_3$, Phys. Rev. B **93**, 195158 (2016).

[36] M. Laubach, J. Reuther, R. Thomale, and S. Rachel, Three-band Hubbard model for Na_2IrO_3: Topological insulator, zigzag antiferromagnet, and Kitaev-Heisenberg material, Phys. Rev. B **96**, 121110(R) (2017).

[37] R. Yadav, S. Rachel, L. Hozoi, J. van den Brink, and G. Jackeli, Strain- and pressure-tuned magnetic interactions in honeycomb Kitaev materials, Phys. Rev. B **98**, 121107(R) (2018).

[38] M. L. Baez, Minimal models of $\alpha-Li_2IrO_3$: Range of interactions, ground state properties, and magnetization processes, Phys. Rev. B **99**, 184436 (2019).

[39] H. Takagi, T. Takayama, G. Jackeli, G. Khaliullin, and S. E. Nagler, Concept and realization of Kitaev quantum spin liquids, Nat. Rev. Phys. **1**, 264 (2019).

[40] J. A. Sears, M. Songvilay, K. W. Plumb, J. P. Clancy, Y. Qiu, Y. Zhao, D. Parshall, and Y.-J. Kim, Magnetic order in $\alpha-RuCl_3$: A honeycomb-lattice quantum magnet with strong spin-orbit coupling, Phys. Rev. B **91**, 144420 (2015).

[41] A. Banerjee, C. A. Bridges, J.-Q. Yan, A. A. Aczel, L. Li, M. B. Stone, G. E. Granroth, M. D. Lumsden, Y. Yiu, J. Knolle, S. Bhattacharjee, D. L. Kovrizhin, R. Moessner, D. A. Tennant, D. G. Mandrus, and S. E. Nagler, Proximate Kitaev quantum spin liquid behaviour in a honeycomb magnet, Nat. Mater. **15**, 733 (2016).

[42] Y. Sizyuk, P. Wölfle, and N. B. Perkins, Selection of direction of the ordered moments in Na_2IrO_3 and $\alpha-RuCl_3$, Phys. Rev. B **94**, 085109 (2016).

[43] A. U. B. Wolter, L. T. Corredor, L. Janssen, K. Nenkov, S. Schönecker, S.-H. Do, K.-Y. Choi, R. Albrecht, J. Hunger, T. Doert, M. Vojta, and B. Büchner, Field-induced quantum criticality in the Kitaev system $\alpha-RuCl_3$, Phys. Rev. B **96**, 041405(R) (2017).

[44] P. Lampen-Kelley, S. Rachel, J. Reuther, J.-Q. Yan, A. Banerjee, C. A. Bridges, H. B. Cao, S. E. Nagler, and D. Mandrus, Anisotropic susceptibilities in the honeycomb Kitaev system $\alpha-RuCl_3$, Phys. Rev. B **98**, 100403(R) (2018).

[45] Y. Kasahara, T. Ohnishi, Y. Mizukami, O. Tanaka, S. Ma, K. Sugii, N. Kurita, H. Tanaka, J. Nasu, Y. Motome, T. Shibauchi, and Y. Matsuda, Majorana quantization and half-integer thermal quantum Hall effect in a Kitaev spin liquid, Nature (London) **559**, 227 (2018).

[46] T. Yokoi, S. Ma, Y. Kasahara, S. Kasahara, T. Shibauchi, N. Kurita, H. Tanaka, J. Nasu, Y. Motome, C. Hickey, S. Trebst, and Y. Matsuda, Half-integer quantized anomalous thermal Hall effect in the Kitaev material candidate $\alpha-RuCl_3$, Science **373**, 568 (2021).

[47] H. K. Vivanco, B. A. Trump, C. M. Brown, and T. M. McQueen, Competing antiferromagnetic-ferromagnetic states in a d(7) Kitaev honeycomb magnet, Phys. Rev. B **102**, 224411 (2020).

[48] S. D. Das, S. Kundu, Z. Zhu, E. Mun, R. D. McDonald, G. Li, L. Balicas, A. McCollam, G. Cao, J. G. Rau, H.-Y. Kee, V. Tripathi, and S. E. Sebastian, Magnetic anisotropy of the alkali iridate Na2IrO3 at high magnetic fields: Evidence for strong ferromagnetic Kitaev correlations, Phys. Rev. B **99**, 081101(R) (2019).

[49] S. N. Gupta, P. V. Sriluckshmy, K. Mehlawat, A. Balodhi, D. K. Mishra, S. R. Hassan, T. V. Ramakrishnan, D. V. S. Muthu, Y. Singh, and A. K. Sood, Raman signatures of strong Kitaev exchange correlations in $(Na_{1-x}Li_x)_2IrO_3$: Experiments and theory, Europhys. Lett. **114**, 47004 (2016).

[50] J. A. Sears, L. E. Chern, S. Kim, P. J. Bereciartua, S. Francoual, Y. B. Kim, and Y.-J. Kim, Ferromagnetic Kitaev interaction and the origin of large magnetic anisotropy in $\alpha-RuCl_3$, Nat. Phys. **16**, 837 (2020).

[51] H. Suzuki, H. Liu, J. Bertinshaw, K. Ueda, H. Kim, S. Laha, D. Weber, Z. Yang, L. Wang, H. Takahashi, K. Fürsich, M. Minola, B. V. Lotsch, B. J. Kim, H. Yavas, M. Daghofer, J. Chaloupka, G. Khaliullin, H. Gretarsson, and B. Keimer, Proximate ferromagnetic state in the Kitaev model material $\alpha-RuCl_3$, Nat. Commun. **12**, 4512 (2021).

[52] A. Banerjee, J. Yan, J. Knolle, C. A. Bridges, M. B. Stone, M. D. Lumsden, D. G. Mandrus, D. A. Tennant, R. Moessner, and S. E. Nagler, Neutron scattering in the proximate quantum spin liquid $\alpha-RuCl_3$, Science **356**, 1055 (2017).

[53] M. Songvilay, J. Robert, S. Petit, J. A. Rodriguez-Rivera, W. D. Ratcliff, F. Damay, V. Balédent, M. Jiménez-Ruiz, P. Lejay, E. Pachoud, A. Hadj-Azzem, V. Simonet, and C. Stock, Kitaev interactions in the Co honeycomb antiferromagnets $Na_3Co_2SbO_6$ and $Na_2Co_2TeO_6$, Phys. Rev. B **102**, 224429 (2020).

[54] C. Kim, J. Jeong, G. Lin, P. Park, T. Masuda, S. Asai, S. Itoh, H.-S. Kim, H. Zhou, J. Ma, and J.-G. Park, Antiferromagnetic Kitaev interaction in $J_{\text{eff}} = 1/2$ cobalt honeycomb materials $Na_3Co_2SbO_6$ and $Na_2Co_2TeO_6$, J. Phys.: Condens. Matter **34**, 045802 (2022).

[55] A. M. Samarakoon, Q. Chen, H. Zhou, and V. O. Garlea, Static and dynamic magnetic properties of honeycomb lattice antiferromagnets $Na_2M_2TeO_6$, M = Co and Ni, Phys. Rev. B **104**, 184415 (2021).

[56] L. Janssen, E. C. Andrade, and M. Vojta, Magnetization processes of zigzag states on the honeycomb lattice: Identifying spin models for $\alpha-RuCl_3$ and Na_2IrO_3, Phys. Rev. B **96**, 064430 (2017).

[57] Y. Sizyuk, C. Price, P. Wölfle, and N. B. Perkins, Importance of anisotropic exchange interactions in honeycomb iridates: Minimal model for zigzag antiferromagnetic order in Na_2IrO_3, Phys. Rev. B **90**, 155126 (2014).

[58] S. M. Winter, Y. Li, H. O. Jeschke, and R. Valentí, Challenges in design of Kitaev materials: Magnetic interactions from competing energy scales, Phys. Rev. B **93**, 214431 (2016).

[59] C. Kim, H.-S. Kim, and J.-G. Park, Spin-orbital entangled state and realization of Kitaev physics in 3d cobalt compounds: A progress report, J. Phys.: Condens. Matter **34**, 023001 (2022).

[60] S. Bhattacharjee, S.-S. Lee, and Y. B. Kim, Spin-orbital locking, Emergent pseudo-spin, and magnetic order in honeycomblattice iridates, New J. Phys. **14**, 073015 (2012).

[61] J. G. Rau, E. K.-H. Lee, and H.-Y. Kee, Spin-orbit physics giving rise to novel phases in correlated systems: Iridates and related materials, Annu. Rev. Condens. Matter Phys. **7**, 195 (2016).

[62] H. Liu and G. Khaliullin, Pseudospin exchange interactions in d^7 cobalt compounds: Possible realization of the Kitaev model, Phys. Rev. B **97**, 014407 (2018).

[63] H. Liu, J. Chaloupka, and G. Khaliullin, Kitaev Spin Liquid in 3*d* Transition Metal Compounds, Phys. Rev. Lett. **125**, 047201 (2020).

[64] R. Sano, Y. Kato, and Y. Motome, Kitaev-Heisenberg Hamiltonian for high-spin d^7 Mott insulators, Phys. Rev. B **97**, 014408 (2018).

[65] C. Wong, M. Avdeev, and C. D. Ling, Zig-zag magnetic ordering in honeycomb-layered $Na_3Co_2SbO_6$, J. Solid State Chem. **243**, 18 (2016).

[66] E. Lefrançois, M. Songvilay, J. Robert, G. Nataf, E. Jordan, L. Chaix, C. V. Colin, P. Lejay, A. Hadj-Azzem, R. Ballou, and V. Simonet, Magnetic properties of the honeycomb oxide $Na_2Co_2TeO_6$, Phys. Rev. B **94**, 214416 (2016).

[67] A. K. Bera, S. M. Yusuf, A. Kumar, and C. Ritter, Zigzag antiferromagnetic ground state with anisotropic correlation lengths in the quasi-two-dimensional honeycomb lattice compound $Na_2Co_2TeO_6$, Phys. Rev. B **95**, 094424 (2017).

[68] G. Lin, J. Jeong, C. Kim, Y. Wang, Q. Huang, T. Masuda, S. Asai, S. Itoh, G. Günther, M. Russina, Z. Lu, J. Sheng, L. Wang, J. Wang, G. Wang, Q. Ren, C. Xi, W. Tong, L. Ling, Z. Liu *et al.*, Field-induced quantum spin disordered state in spin-1/2 honeycomb magnet $Na_2Co_2TeO_6$, Nat. Commun. **12**, 5559 (2021).

[69] H. Liu, Towards Kitaev spin liquid in 3*d* transition metal compounds, Int. J. Mod. Phys. B **35**, 2130006 (2021).

[70] S. Rachel, L. Fritz, and M. Vojta, Landau Levels of Majorana Fermions in a Spin Liquid, Phys. Rev. Lett. **116**, 167201 (2016).

[71] B. Perreault, S. Rachel, F. J. Burnell, and J. Knolle, Majorana Landau-level Raman spectroscopy, Phys. Rev. B **95**, 184429 (2017).

[72] R. Berthelot, W. Schmidt, A. W. Sleight, and M. A. Subramanian, Studies on solid solutions based on layered honeycomb-ordered phases P2-$Na_2M_2TeO_6$ (M=Co, Ni, Zn), J. Solid State Chem. **196**, 225 (2012).

[73] D. Yu, R. Mole, T. Noakes, S. Kennedy, and R. Robinson, Pelican – a time of flight cold neutron polarization analysis spectrometer at OPAL, J. Phys. Soc. Jpn. **82**, SA027 (2013).

[74] D. Yu, R. A. Mole, and G. J. Kearley, Performance test on PELICAN – a multi-purpose time of flight cold neutron spectrometer, EPJ Web Conf. **83**, 03019 (2015).

[75] D. Richard, M. Ferrand, and G. J. Kearley, Analysis and visualisation of neutron-scattering data, J. Neutron Res. **4**, 33 (1996).

[76] W. Chen, X. Li, Z. Hu, Z. Hu, L. Yue, R. Sutarto, F. He, K. Iida, K. Kamazawa, W. Yu, X. Lin, and Y. Li, Spin-orbit phase behavior of $Na_2Co_2TeO_6$ at low temperatures, Phys. Rev. B **103**, L180404 (2021).

[77] W. Yao and Y. Li, Ferrimagnetism and anisotropic phase tunability by magnetic fields in $Na_2Co_2TeO_6$, Phys. Rev. B **101**, 085120 (2020).

[78] P. A. Maksimov and A. L. Chernyshev, Rethinking $\alpha-RuCl_3$, Phys. Rev. Research **2**, 033011 (2020).

[79] R. L. Smit, S. Keupert, O. Tsyplyatyev, P. A. Maksimov, A. L. Chernyshev, and P. Kopietz, Magnon damping in the zigzag phase of the Kitaev-Heisenberg-Γ model on a honeycomb lattice, Phys. Rev. B **101**, 054424 (2020).

[80] S. M. Winter, K. Riedl, P. A. Maksimov, A. L. Chernyshev, A. Honecker, and R. Valentí, Breakdown of magnons in a strongly spin-orbital coupled magnet, Nat. Commun. **8**, 1152 (2017).

[81] R. E. Watson and A. J. Freeman, Hartree-Fock atomic scattering factors for the iron transition series, Acta. Cryst. **14**, 27 (1961).

[82] A. Banerjee, P. Lampen-Kelley, J. Knolle, C. Balz, A. A. Aczel, B. Winn, Y. Liu, D. Pajerowski, J. Yan, C. A. Bridges, A. T. Savici, B. C. Chakoumakos, M. D. Lumsden, D. A. Tennant, R. Moessner, D. G. Mandrus, and S. E. Nagler, Excitations in the field-induced quantum spin liquid state of $\alpha-RuCl_3$, npj Quantum Mater. **3**, 8 (2018).

[83] A. T. Boothroyd, P. Babkevich, D. Prabhakaran, and P. G. Freeman, An hour-glass magnetic spectrum in an insulating, hole-doped antiferromagnet, Nature (London) **471**, 341 (2011).

[84] Y. Drees, Z. W. Li, A. Ricci, M. Rotter, W. Schmidt, D. Lamago, O. Sobolev, U. Rütt, O. Gutowski, M. Sprung, A. Piovano, J. P. Castellan, and A. C. Komarek, Hour-glass magnetic excitations induced by nanoscopic phase separation in cobalt oxides, Nat. Commun. **5**, 5731 (2014).

[85] A. Katanin and O. P. Sushkov, Quasielastic neutron scattering from two-dimensional antiferromagnets at a finite temperature, Phys. Rev. B **83**, 094426 (2011).

[86] S. M. Winter, A. A. Tsirlin, M. Daghofer, J. v. d. Brink, Y. Singh, P. Gegenwart, and R. Valenti, Models and materials for generalized kitaev magnetism, J. Phys.: Condens. Matter **29**, 493002 (2017).

[87] X. Hong, M. Gillig, R. Hentrich, W. Yao, V. Kocsis, A. R. Witte, T. Schreiner, D. Baumann, N. Pérez, A. U. B. Wolter, Y. Li, B. Büchner, and C. Hess, Strongly scattered phonon heat transport of the candidate Kitaev material $Na_2Co_2TeO_6$, Phys. Rev. B **104**, 144426 (2021).